The Astronomical Journal, 159:204 (15pp), 2020 May https://doi.org/10.3847/1538-3881/ab7b78

Into the UV: A Precise Transmission Spectrum of HAT-P-41b Using *Hubble*'s WFC3/UVIS G280 Grism

H. R. Wakeford[1,2], D. K. Sing[3,4], K. B. Stevenson[5], N. K. Lewis[6], N. Pirzkal[2], T. J. Wilson[2,7], J. Goyal[6], T. Kataria[8], T. Mikal-Evans[9], N. Nikolov[4], and J. Spake[10]

[1] School of Physics, University of Bristol, H.H. Wills Physics Laboratory, Tyndall Avenue, Bristol BS8 1TL, UK; stellarplanet@gmail.com
[2] Space Telescope Science Institute, 3700 San Martin Drive, Baltimore, MD 21218, USA
[3] Department of Earth & Planetary Sciences, Johns Hopkins University, Baltimore, MD, USA
[4] Department of Physics & Astronomy, Johns Hopkins University, Baltimore, MD, USA
[5] JHU Applied Physics Laboratory, 11100 Johns Hopkins Road, Laurel, MD 20723, USA
[6] Department of Astronomy and Carl Sagan Institute, Cornell University, 122 Sciences Drive, Ithaca, NY 14853, USA
[7] University of Exeter, Physics Building, Stocker Road, Exeter EX4 4QL, UK
[8] NASA Jet Propulsion Laboratory, 4800 Oak Grove Drive, Pasadena, CA 91109, USA
[9] Kavli Institute for Astrophysics and Space Research, Massachusetts Institute of Technology, 77 Massachusetts Avenue, 37-241, Cambridge, MA 02139, USA
[10] Division of Geological and Planetary Sciences, California Institute of Technology, Pasadena, CA 91125, USA

Received 2020 January 22; revised 2020 February 27; accepted 2020 February 29; published 2020 April 13

Abstract

The ultraviolet–visible wavelength range holds critical spectral diagnostics for the chemistry and physics at work in planetary atmospheres. To date, time-series studies of exoplanets to characterize their atmospheres have relied on several combinations of modes on the *Hubble Space Telescope*'s STIS/COS instruments to access this wavelength regime. Here for the first time, we apply the *Hubble* WFC3/UVIS G280 grism mode to obtain exoplanet spectroscopy from 200 to 800 nm in a single observation. We test the G280 grism mode on the hot Jupiter HAT-P-41b over two consecutive transits to determine its viability for the characterization of exoplanet atmospheres. We obtain a broadband transit depth precision of 29–33 ppm and a precision of on average 200 ppm in 10 nm spectroscopic bins. Spectral information from the G280 grism can be extracted from both the positive and negative first-order spectra, resulting in a 60% increase in the measurable flux. Additionally, the first *Hubble Space Telescope* orbit can be fully utilized in the time-series analysis. We present detailed extraction and reduction methods for use by future investigations with this mode, testing multiple techniques. We find the results to be fully consistent with STIS measurements of HAT-P-41b from 310 to 800 nm, with the G280 results representing a more observationally efficient and precise spectrum. HAT-P-41b's transmission spectrum is best fit with a model with $T_{\rm eq} = 2091$ K, high metallicity, and significant scattering and cloud opacity. With these first-of-their-kind observations, we demonstrate that WFC3/UVIS G280 is a powerful new tool to obtain UV–optical spectra of exoplanet atmospheres, adding to the UV legacy of *Hubble* and complementing future observations with the *James Webb Space Telescope*.

Unified Astronomy Thesaurus concepts: Exoplanet atmospheres (487); Near ultraviolet astronomy (1094); Hubble Space Telescope (761)

1. Introduction

The characterization of planetary atmospheres in the solar system and beyond has long leveraged the ultraviolet (UV) to near-infrared (NIR) spectroscopic capabilities of the *Hubble Space Telescope* (*HST*). Observations with *HST* have been critical in the exploration of the chemical composition, climate, and aerosol properties of exoplanet atmospheres (see Kreidberg et al. 2018, and references therein). With the help of *HST* we now know that clouds and hazes are likely present in all types of exoplanetary atmospheres (e.g., Marley et al. 2013; Helling 2019; Wakeford et al. 2019), but we currently lack information related to their abundances, physical properties, and extent throughout the atmosphere. We also know that exoplanets exhibit extended upper atmospheres with evidence for atmospheric escape (e.g., Ehrenreich et al. 2014; Bourrier et al. 2018; Sing et al. 2019), but struggle to connect physical processes in the lower and upper portions of exoplanet atmospheres.

The UV through optical (200–800 nm) spectra of planets hold rich information about the chemistry and physics at work across a broad range of atmospheric pressures. In the solar system, UV and near-UV spectroscopy has been critical in identifying and measuring the abundances of a variety of hydrocarbon and sulfur-bearing species, produced via photochemical mechanisms, as well as oxygen and ozone and more. For exoplanets, UV to near-UV spectroscopy has been especially useful for constraining aerosol properties and exploring atmospheric chemistry in hot (>1000 K) atmospheres (e.g., Sing et al. 2016; Evans et al. 2018). To date, only a handful of exoplanets have been probed in the critical 200–400 nm wavelength range that crosses the optical to UV boundary. Results from these studies have been mixed, limited by the wavelength coverage and sensitivity of the workhorse instrument for such studies, *HST*'s Space Telescope Imaging Spectrograph (STIS) G430L and E230M gratings.

It is important to remember that none of *HST*'s instruments or modes were specifically designed to support exoplanet observations. It has only been through the development of new observational strategies, such as spatial scanning (McCullough & MacKenty 2012; McCullough et al. 2014), and data reduction techniques that the potential for *HST* to probe exoplanet atmospheres has been achieved. In general, slitless spectroscopic observing modes have been preferred for high-precision time-series observations of exoplanets that transit (pass in front of) their host stars because they typically offer more throughput and temporal stability. The slitless spectroscopy capabilities of *HST*'s Wide Field Camera 3 (WFC3) have been heavily used by the exoplanet community at infrared wavelengths (750–1800 nm) with the G102 and G141 grisms. However, *HST*'s WFC3 UV/visible (UVIS) channel also offers slitless spectroscopy in the UV through visible (200–800 nm) wavelength range that has yet to be leveraged for exoplanet observations. In fact, this mode has only been employed in a handful of scientific investigations, and was first used as part of *HST* WFC3 early-release science programs in cycle 16 (2006), but none of the G280 work was published from this study.

Here we detail for the first time the observations, spectral extraction, and analysis processes taken to apply *Hubble*'s WFC3/UVIS G280 spectroscopic grism to transiting exoplanet observations. We first introduce the challenges in using the UVIS G280 grism in Section 2. In Section 3 we detail the observations and spectral extraction procedures used. We then detail the broadband time-series analysis using two systematic reduction techniques in Section 4. We use *Spitzer* transit observations to refine system parameters and update the orbital ephemeris in Sections 4.1 and 4.2. We outline the spectroscopic analysis in Section 5 and discuss the results in Section 6 including searching for evidence of atmospheric escape and comparisons to STIS data. We then conclude with a summary of our results and the potential of WFC3/UVIS G280 for future exoplanet investigations.

2. Introduction to the UVIS G280 Grism

The WFC3 instrument on *HST* is fitted with two channels, UVIS and IR. Across these two channels are three slitless spectroscopic grisms: G280 in UVIS and G102 and G141 in the IR channel. The IR grisms have been extensively applied to studies of exoplanet atmospheres with increasing success at the advent of spatial scanning (McCullough & MacKenty 2012), where *HST* slews in the cross-dispersion direction to spread the target light over a column of pixels (e.g., Deming et al. 2013; Wakeford et al. 2013, 2016; Kreidberg et al. 2014; de Wit et al. 2016). However, the UVIS G280 grism has not had such usage despite large throughput in the near-UV (NUV) and wide coverage from 200 to 800 nm. More commonly, studies that cover 300–900 nm are conducted with multiple observations using *HST*'s STIS G430L and G750L low-resolution gratings from 300 to 550 nm and 500 to 900 nm respectively (e.g., Nikolov et al. 2014; Sing et al. 2016; Lothringer et al. 2018) despite their comparatively low throughput (Figure 1).

The UVIS grism, however, comes with several quirks that make it difficult to observe with and challenging to analyze. A number of these challenges will also affect observations with the *James Webb Space Telescope*'s (*JWST*) spectroscopic instrument modes. Therefore, WFC3/UVIS G280 is a current working example of the challenges that will be faced with *JWST*. Here we detail each of the challenges associated with WFC3's UVIS grism and also the advantages it has over other instrument modes in the NUV to optical wavelengths.

2.1. Challenges

We detail some of the challenges encountered with this data set and those expected in the general use of this instrument mode for exoplanet time-series characterization.

Curved spectral trace. The trace for spectral order with the G280 grism is strongly curved at shorter wavelengths. The trace is best fit with a sixth-order polynomial function detailed by Pirzkal et al. (2017) and Section 3. This curvature causes it to be offset in the cross-dispersion direction from the zeroth-order position, meaning that subarray sizes need to be carefully chosen. Unlike the IR grisms, the spectra should not be spatially scanned because this would result in overlapping wavelength regions along the scan direction.

The curved spectral trace also introduces a nonlinear wavelength solution, meaning each pixel has a slightly different wavelength range than the surrounding pixels in that column. The wavelength solution is therefore extracted relative to the fitted trace position on the detector with a sixth-order polynomial.

Multiple overlapping orders. Additional spectral orders, both positive and negative, overlap with the first-order spectra at wavelengths greater than 550 nm. In many cases these additional orders will be much dimmer than the first-order spectrum and not impact the observations. However, for stars bright in the NUV, such as those of types O, B, and A, the additional spectral orders may impact the spectral extraction.

In the presented case, the second-order spectrum is ≈65× dimmer than the primary spectrum in both positive and negative orders. This would negligibly contribute to the measured transit depths, causing the measured planetary radius (R_m) to be ≈99.24% of the true planetary radius (R) following

$$\frac{R_m}{R} = \sqrt{\frac{1}{1+\frac{1}{65}}} = 0.9924. \tag{1}$$

Geometric distortion. Using the grism filters causes the spectra to be offset spatially in the detector relative to their direct image X and Y coordinates. For the UVIS array the offset varies as a function of the position due to geometric distortion (Rothberg et al. 2011). The relationship between the coordinates in x and y pixel position also needs to be taken into account when planning the observations in X and Y arcsecond coordinates (see WFC3 data handbook for conversion functions[11]).

Orientation constraints. The spectral traces of the positive and negative orders extend across more than 500 pixels each, depending on the brightness of the target. In a crowded field or where a target is part of a visual binary system, tight constraints need to be placed on the orientation of the observations to prevent contamination from nearby stars. This is often mitigated in WFC3/IR grism observations using spatial scans, where the spectra can be extracted by differencing the individual non-destructive reads within the final science frame. However, as WFC3/UVIS grism observations can only be conducted in stare mode, up-the-ramp sampling cannot be used to recover overlapping spectra.

Cosmic rays. The large wavelength coverage that extends significantly into the blue wavelengths increases the number of detected comic rays compared to the IR detectors.

JWST challenges. For *JWST* a number of the instrument modes that will be utilized for exoplanet time-series data exhibit curved spectral traces, overlapping spectral orders, and contamination constraints from additional sources on the sky. NIRISS SOSS mode is most similar to the G280 grism with both strongly curved spectral traces and overlapping spectral

[11] WFC3 Data Handbook Appendix C.2 (https://hst-docs.stsci.edu/display/WFC3IHB/C.2+WFC3+Patterns).

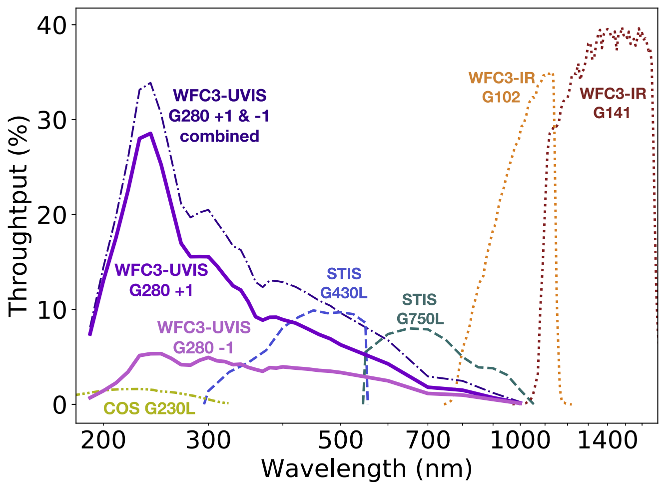

Figure 1. Throughput curves for *HST* instruments and modes commonly used for exoplanet time-series observations. Solid lines are the WFC3-UVIS G280 grism orders +1 and −1; the dark dotted–dashed line is the combined transmission of both orders. Dashed lines are STIS G430L and G750L gratings. The -..- line shows the COS G230L. Dotted lines are WFC3-IR G102 and G141 grisms.

orders. It is also expected that NIRSpec Bright Object Time Series observations will have a slightly curved trace. For all slitless modes on *JWST* used for exoplanet time-series observations contamination overlap will need to be carefully considered and orientation constraints carefully sampled.

2.2. Advantages

While we have detailed many challenges there are also significant advantages to this instrument over other modes in the NUV and optical. We detail these here.

Wide wavelength coverage. Observations are conducted over the whole wavelength range 200–800 nm in a single exposure. Low-resolution spectra across this wide range can address the two main exoplanet science points revealed by *HST* observations: cloud opacities and atmospheric escape. The G280 grism can measure the lower atmosphere sensitive to aerosol scattering, while signatures of large atmospheric escape can be detectable in narrow bands around strong Fe and Mg signatures at <300 nm.

Multiple spectral orders. Both the positive and negative orders are measured in each exposure. The UVIS CCD is split into two chips (1 and 2), with each chip of 2051 × 2048 pixels easily encompassing both spectral orders, which each cover ≈500 pixels in the dispersion direction. In the presented observations we use chip 2 because it has been shown to be more stable than chip 1. We therefore also recommend the use of chip 2 for future studies.

Throughput. WFC3/UVIS has the highest throughput among all *HST* instruments in the wavelength range from its lower cut off at 200 nm to the upper end at ∼800 nm. The throughput of UVIS G280 in the NUV is on average 25 times that of STIS E230M between 200 and 400 nm, and roughly four times that of STIS G430L at 350 nm. UVIS G280 also has the advantage of being able to measure both positive and negative spectral orders that have a combined throughput greater than STIS G430L across the whole wavelength range (see Figure 1).

New calibration program. Prior to these observations there have been three instrument science reports (Kuntschner et al. 2009; Rothberg et al. 2011; Pirzkal et al. 2017) and no scientific papers using this grism. Demand for time-series observations with this grism has increased and there are now new calibration programs being implemented to better characterize the detector and improve the trace fitting for all spectral orders. Calibration of the instrument and mode are important to understand the structure of the CCD, on-sky changes in the point-spread function (PSF), and wavelength dispersion across the detector—especially under the Requirements of long-term stability for exoplanet investigations that span multiple *HST* orbits.

Overall the WFC3/UVIS G280 grism has many challenges that are difficult but not impossible to overcome, and a significant advantage over other instrument modes in this wavelength range. In the following sections we detail the observations taken and the measurements made with the tools to overcome these challenges.

3. UVIS G280 Observations

We used *HST*'s WFC3/UVIS channel with the G280 spectroscopic slitless grism to observe the spectrum of the transiting exoplanet host star HAT-P-41 from 200 to 800 nm (GO-15288, PIs D.K. Sing & N.K. Lewis). Unlike the WFC3/IR G102 and G141 grisms, the UVIS G280 grism produces a spectrum that is strongly curved, with overlapping spectral orders at longer wavelengths, and a −1 order spectrum that is dimmer (∼60%) than the +1 order. We designed an observation strategy that would cover both +1 and −1 orders simultaneously to examine this difference in flux and test the usability of the G280 grism for time-series exoplanet studies.

We observed the target HAT-P-41, in the constellation of Aquila, over two visits, each consisting of five *HST* orbits, to measure the transit of the hot Jupiter exoplanet HAT-P-41b. The two visits were separated by a single planetary orbital period (visit 1: 2018 August 1; visit 2: 2018 August 4, period = 2.694047 days), significantly reducing the potential impact of any stellar variations on the transits of this quiet F6 star.

Each visit consists of 54 exposures, over five *HST* orbits, with exposure times of 190 s. We used a 2100 × 800 subarray, with a POS TARG *Y* offset of −50″ to center the spectrum on chip 2. The subarray is cut out of the full 2051 × 4096 pixel CCD that contains chips 1 and 2, where chip 1 and chip 2 are separated by 1.″2. Our target star, HAT-P-41, has a nearby companion separated by 3.″615, equivalent to ≈91.5 pixels on the detector. The nearby companion resulted in a number of tight orientation constraints on the observation. However, our subarray is large enough to capture both full +1 and −1 spectral orders around the zeroth-order trace. The maximum flux obtained in a single pixel in the spectral trace is ≈36,000 e^-, keeping it well within the saturation and nonlinearity limit of the detector, which is approximately 67,000–72,000 e^- (Gilliland et al. 2010).

3.1. Spectral Extraction

The spectral traces for both visits and both +1 and −1 orders were extracted using calibration files provided by the WFC3 team. A complete extraction and reduction of the provided data requires the following steps: (a) cosmic-ray removal, (b) background subtraction, (c) aperture determination, and (d) trace fitting. We then use the WFC3 UVIS calibration files to compute the wavelength solution for each spectral order. We

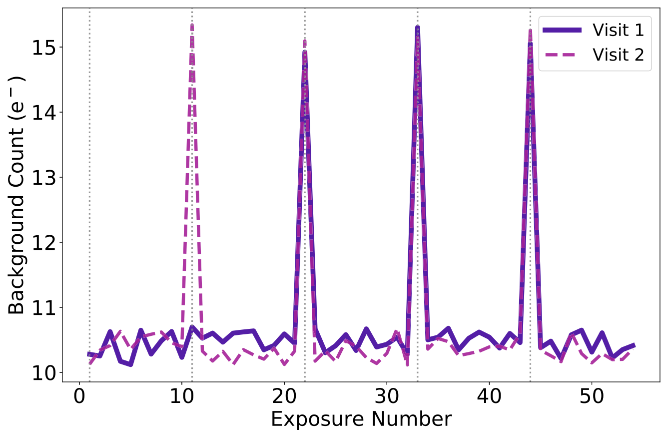

Figure 2. Modal background count for each exposure in visit 1 (solid) and visit 2 (dashed) across the whole subarray. The dotted vertical lines indicate the start of a new *HST* orbit. The background is higher at the start of each *HST* orbit with a bimodal distribution, perhaps due to stray earthshine or orbital effects on the telescope.

also performed spectral extraction with IRAF and custom IDL routines as a second check on the extraction procedure because this is the first published analysis of G280 grism data for time-series spectroscopy (see Section 3.1.1 for details).

Cosmic-ray removal. We used the "flt" files from the *Calwfc3* pipeline to analyze each exposure. Cosmic rays were then rejected by examining the time series for each pixel, and flagging and replacing 3.5σ outliers in an iterative process. We also applied a further spatial cosmic-ray cleaning step by rejecting cosmic rays through Laplacian edge detection (van Dokkum 2001). We did a final cosmic-ray cleaning on the extracted 1D stellar spectra by comparing them to the median combined spectra and replacing outliers that deviated by more than 3.5σ. Where cosmic rays are flagged temporally we replace the pixel value with a median of the time-sampled pixel; where they are flagged spatially a median of the surrounding pixels in the same frame is used.

Background subtraction. We use the local background estimation, similar to *Wide-field Infrared Survey Explorer* (*WISE*) (see Section 4.4 c of Cutri et al. 2012 [12]), by computing the pixel mode for each image and subtracting that from each pixel. The mode, or most common binned histogram value, tends to be robust against the bright tail of the distribution that is caused by other stars and cosmic-ray (or hot) pixels in the exposure. We compared this to the mean and median σ-clipped pixel values and found good agreement, giving weight to the mode being resistant to outliers. In each visit the first exposure of each orbit has much higher background than the other exposures, with a slightly bimodal distribution around the peak of the histogram (see Figure 2), perhaps due to stray earthshine or orbital effects on the telescope. We remove the first exposure of each orbit in both visits in the light-curve analysis.

Figure 3 shows the visual difference between the original "flt" images and a cleaned, background-subtracted exposure. We save the cleaned and background-subtracted images as FITS files to be used for the trace fitting routines.

Trace fitting. To extract the target spectrum using the provided calibration files for UVIS G280,[13] the subarray image needs to be re-embedded into the full frame (Rothberg et al. 2011). This can be done using the EMBEDSUB routine in WFC3TOOLS.[14] This routine also requires the "spt" files be downloaded from the MAST database and contained within the same folder as the cleaned FITS files generated from the previous steps.

Direct images of the target were taken with the F300X filter at the start of each visit to provide an accurate location of our target on the detector. Visits 1 and 2 were positioned on the detector within 1 pixel of each other with x, y centroid positions of [2040.8756, 1063.8825] and [2041.0399, 1062.9073] respectively.

Using the description of the spectral trace of the G280 UVIS grism from Pirzkal et al. (2017), we computed the expected location of the trace in each exposure of our G280 data sets. In summary, Pirzkal et al. (2017) compute the trace location as a function of the x-pixel on the detector and a high-order 2D polynomial is fit across the trace. The best-fit trace is defined by a sixth-order polynomial function with a linear 2D field dependence. The reference column for the polynomial fit is chosen to be close to the inflection point of the trace to ensure the best fit to both the highly curved spectrum at short wavelengths and the near-linear trace at longer wavelengths. The polynomial function reproduces the position of both the +1 and −1 spectral orders to within a fraction of a pixel from 200 to 800 nm. Figure 4 shows the central trace position for both visits and computed for the +1 and −1 spectral orders. The trace fits are currently best calibrated to the +1 order; however, the authors note that there is a new WFC3/UVIS G280 calibration program that will fully characterize the −1 and additional spectral orders. At longer wavelengths, toward the tail end of the spectral trace, fringing effects come into play that divert the spectra from the fit polynomial trace (see Figure 5).

A simple extraction of the spectrum contained in each data set was created by adding up the observed count rates in pixels above and below the computed location of the trace. We tested apertures ranging from ±5 pixels around the central trace to ±50 pixels. To determine the best aperture we minimized the standard deviation of the residuals for out-of-transit counts. We find that the optimal aperture is ±12 pixels (see Figure 4), to account for the slightly extended wings of the trace (Kuntschner et al. 2009). Both the +1 and −1 spectral orders were processed in this manner.

The overlapping spectral orders are expected to impact the spectrum at long wavelengths beyond approximately 400 nm. However, these observations were not ideal to show the impact of overlapping spectral orders because the star is too dim in the shorter wavelengths, ≈65× dimmer than the first-order trace. We discuss potential corrections to this in more detail in Section 5.

Wavelength solution. The wavelength solution is calculated from the trace position using the equation detailed in Pirzkal et al. (2017), which is calibrated from 190 to 800 nm. The extracted wavelength solution is good to ±0.7 nm, which is roughly half of a UVIS resolution element. We measure the mean spectral dispersion in the first order, which varies from ∼1.1 to 1.6 nm per pixel over the full spectral range 200–800 nm.

We plot the stellar spectra for both visits and first-order spectra in Figure 5, showing the 16–84 percentile range of each spectrum with remarkable agreement between visits, demonstrating the stability of the instrument. Beyond 800 nm the target spectrum shows extreme fringing effects and is not

[12] *WISE* All-sky release explanatory supplement, Section 4.4 c (http://wise2.ipac.caltech.edu/docs/release/allsky/expsup/sec4_4c.html).
[13] G280 UVIS grism files (http://www.stsci.edu/hst/instrumentation/wfc3/documentation/grism-resources).
[14] https://github.com/spacetelescope/wfc3tools

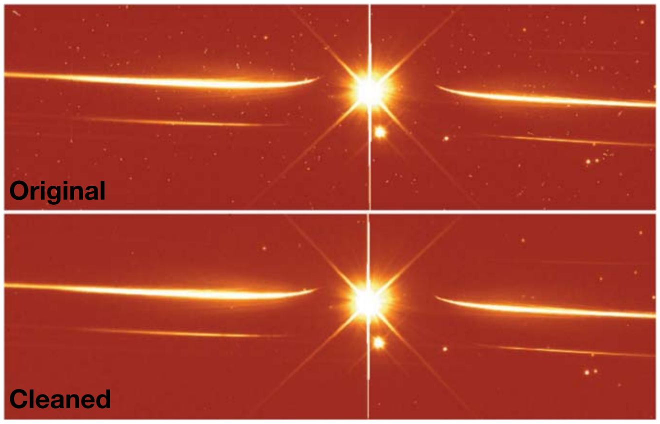

Figure 3. *HST* WFC3/UVIS G280 spectral image. Top: "flt" file processed and available on the MAST archive. Bottom: cleaned file with cosmic rays and hot pixels removed, and flat-fielding applied. In this comparison one can clearly see the difference between the original and cleaned data, demonstrating the requirement for accurate and precise treatment of detector artifacts and cosmic-ray hits.

calibrated; thus we remove it from this analysis. It is also clear to see that the −1 order is significantly dimmer across the whole wavelength range with a large impact on the short wavelengths, short of 250 nm, where the flux drops almost to zero.

3.1.1. IRAF APALL Spectral Extraction

We also performed spectral extraction with IRAF and custom IDL routines. The images were first background-subtracted and cosmic rays were removed in the same way as detailed above. We then used IRAF's APALL routine to extract the spectra for each image in the time series, finding that an eighth-order Legendre polynomial was optimal for the spectral trace extraction as measured by the trace rms residuals. We note that with IRAF, the fixed aperture center varies smoothly to follow changes in the position of the spectrum across the dispersion axis, and partial pixels are used at the ends. We extracted the spectra with a wide range of aperture sizes, finding that a 24 pixel aperture was optimal. Similar to the UVIS calibration pipeline routines, the extracted spectra still exhibited a few cosmic rays not cleaned in previous processes; we also then perform the cosmic-ray removal step for 1D stellar spectra. Using IRAF APALL we were unable to replicate the calculation of the wavelength solution and therefore used the solution calculated following Pirzkal et al. (2017) that required the trace fitting following the UVIS calibration pipeline.

The two spectral extraction techniques produce near identical stellar spectra and transmission spectra. However, in the following sections we adopt and present the analysis based on the spectra extracted using the UVIS calibration pipeline because it is a widely accessible, publicly available extraction method that does not rely on proprietary custom routines, and has a fully consistent wavelength solution.

4. Broadband White-light Analysis

Prior to measuring the transmission spectrum of HAT-P-41b, we first analyze the broadband white-light curve from 200 to 800 nm. In this section we detail the analysis of the broadband white-light transit depth measured in the UVIS G280 transits for each visit and spectral order based on two different systematic treatment methods—instrument systematic marginalization (Wakeford et al. 2016) and jitter decorrelation (Sing et al. 2019).

Instrument systematic marginalization uses a pseudo-stochastic grid of corrective systematic models to measure the desired light-curve parameters, namely the transit depth, via an evidence-based weight assigned by the data to each potential systematic model. We run a grid of 50 systematic models in the form of an extended polynomial:

$$S(\boldsymbol{x}) = t_1\phi_t \times \sum_{i=1}^{n} p_i \phi_{HST}^{i} \times \sum_{j=1}^{n} l_j \delta_\lambda^{j} + 1 \tag{2}$$

where ϕ_t is the planetary phase representing a linear slope over the whole visit, ϕ_{HST} is the *HST* orbital phase accounting for "*HST* thermal breathing" effects, and δ_λ is the positional shift in the wavelength direction on the detector over the visit. Each of these parameters has a scaling factor with the linear slope defined by t_1, and "*HST* breathing" and positional shifts fit up to a fourth-order polynomial function defined by p_{1-n} and l_{1-n}, respectively. Each of the scaling parameters is then either fit as a free parameter to activate the systematic model or fixed to zero. The whole grid of 50 systematic models used in this analysis can be found in Table 2 of Wakeford et al. (2016)—note that the table is 0 indexed.

We approximate the evidence (marginal likelihood) of each systematic model fit to the data using the Akaike information criterion (AIC). We then calculate the evidence-based weight (W_q) across all 50 systematic models and use the information from all models to marginalize over the desired parameter (α_q):

$$\alpha_m = \sum_{q=0}^{N_q} (W_q \times \alpha_q), \tag{3}$$

which is Equation (15) of Wakeford et al. (2016), where N_q is the number of models fit and α_m is the resulting marginalized parameter. The uncertainty is then calculated in a similar way based on the weights (see Equation (16) of Wakeford et al. 2016).

Jitter decorrelation uses *HST*'s Pointing Control System to detrend photometric time-series data. Based on the results of Sing et al. (2019), we include optical state vectors traditionally used for STIS (Sing et al. 2011) as well as several jitter vectors. The full systematics model, $S(\boldsymbol{x})$, used to detrend the light curve is written as

$$\begin{aligned} S(\boldsymbol{x}) = {} & p_1\phi_t + \textstyle\sum_{i=1}^{4} p_{i+1}\phi_{HST}^{i} + p_6\delta_\lambda \\ & + p_7 X_{\rm psf} + p_8 Y_{\rm psf} + p_9 \text{R.A.} + p_{10}\text{decl.} \\ & + p_{11} Vn_{\rm roll} + p_{12} Vt_{\rm roll} + 1, \end{aligned} \tag{4}$$

where ϕ_t is a linear baseline time trend, ϕ_{HST} is the 96 minute *HST* orbital phase, $X_{\rm psf}$ and $Y_{\rm psf}$ are the detector positions of the PSF as measured by the spectral trace, δ_λ is the wavelength shift of each spectrum as measured by cross-correlation, *V2*_roll and *V3*_roll are roll of the telescope along the *V2* and *V3* axes, R.A. and decl. are the R.A. and decl. of the aperture reference, and $p_{1,\ldots,12}$ are the fit systematic parameter coefficients. The first portion of this function was found to be the best functional form of the additional systematic features and corresponds to one of the models used in the marginalization grid. This function is then fit for all transit light curves

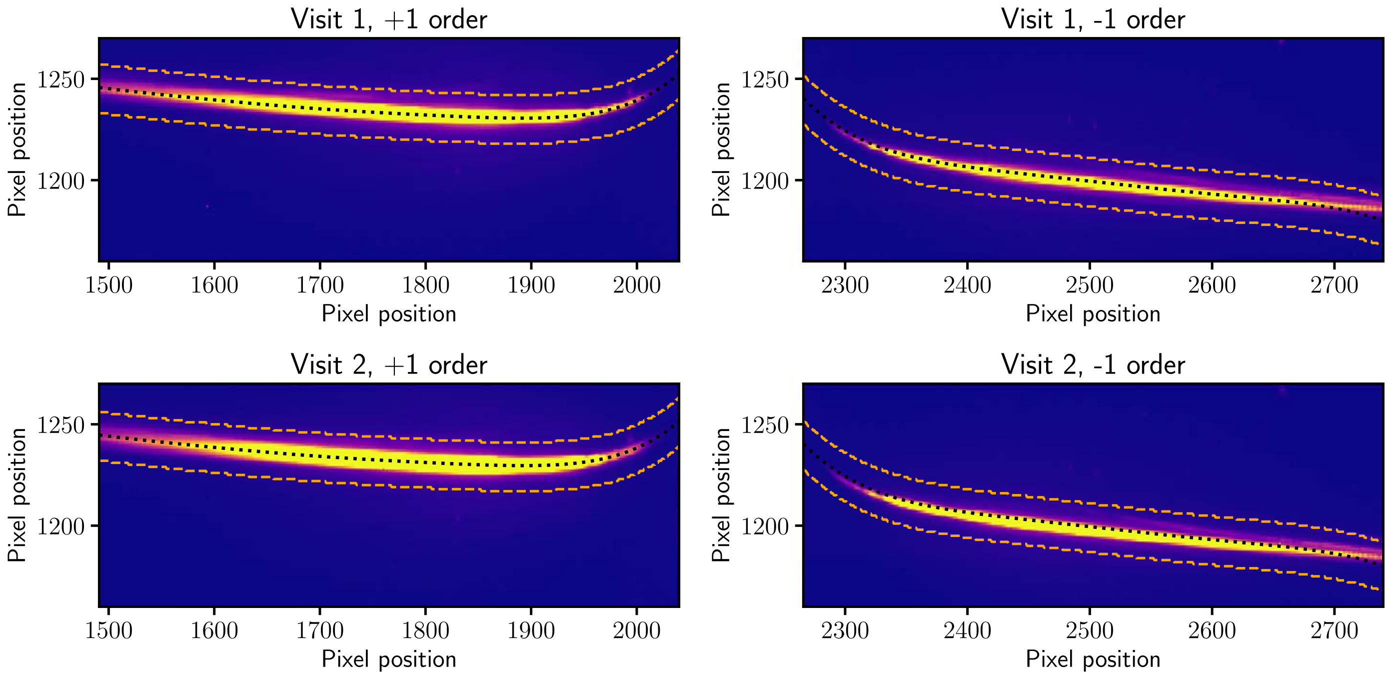

Figure 4. *HST* WFC3/UVIS G280 spectral image. Top: visit 1, +1 spectral order (left) and −1 spectral order (right). Bottom: visit 2, +1 spectral order (left) and −1 spectral order (right). All images are background-subtracted and cosmic rays have been removed. The dotted black line shows the calculated trace center, with the extent of the ±12 pixel aperture shown by orange dashed lines. At lower flux values the spectral trace does not fit quite as well but the full flux is captured inside the selected aperture. Color shows flux, truncated at 25 e^{-} s^{-1}.

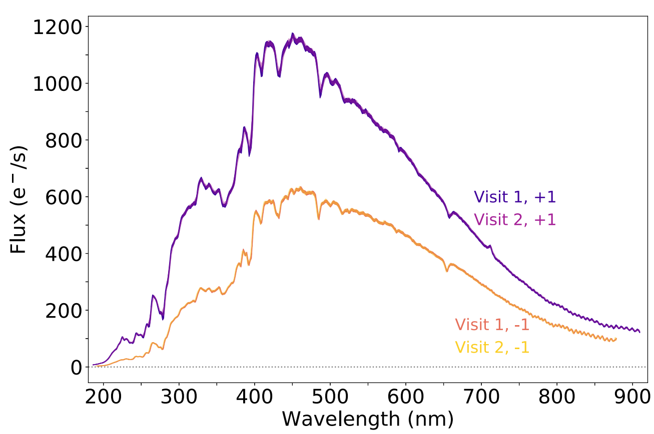

Figure 5. The 16–84 percentile range of the spectral trace of each visit and each order. The +1 orders and −1 orders overlap closely, making it difficult to tell the two visits apart and demonstrating the stability of the instrument and the star. The −1 orders are ∼50% dimmer than the +1 orders, with little to no flux short of 250 nm. Beyond 800 nm fringing patterns can clearly be seen in the stellar spectra and we do not use these wavelengths for the light-curve analysis.

in this form and is not marginalized over to determine the optimal functional form in each light curve. The full jitter decorrelation set results in a total of up to 12 terms used to describe the instrument systematics of the data set in question. However, in practice not all of these parameters are needed. For each visit and each of the two orders, we used the AIC and measured red noise, σ_r, to determine the optimal optical state vectors to include from the full set without overfitting the data and minimizing the red noise.

Both systematic marginalization and jitter decorrelation require a measurement of the changes in spectral position on the detector across the duration of the observation (δ_λ). To calculate the shift, we cross-correlate the 1D stellar spectra to a template spectrum and measure the displacement across the whole wavelength range. To demonstrate that this accurately represents the physical shift on the detector, we measured the position for three background sources distributed across the exposure image. We selected the most Gaussian-like sources from the full image and used a 2D Gaussian fit to their zeroth-order spectrum in each exposure of each visit. In this case we cannot use the zeroth order of the target or its stellar companion to measure this shift because they are both saturated on the detector. Figure 6 shows δ_λ for visits 1 and 2 measured using the cross-correlation method (Cc) and the range of positional values measured from the three background sources (stars). The positional shifts are very similar in form, with the vertical breaks showing where the telescope is reset after each *HST* orbit. The magnitude of the positional shifts is on the sub-pixel scale and is easily accounted for with either of the systematic treatments detailed. Using the 2D Gaussian fit to the background sources, we find that positional shifts in the y-direction are negligible and do not improve the fit to the data.

Due to the phase coverage of *HST* observations, resulting from Earth occultation events, we are unable to accurately fit for the inclination, a/R_*, and orbital period of the system. Unfortunately, HAT-P-41b was not observed by the *Transiting Exoplanet Survey Satellite*, which would have allowed us to easily constrain the system parameters. To fit for these vital parameters we instead use two transit observations from the *Spitzer Space Telescope* IRAC instrument to obtain accurate system parameters for the inclination and a/R_* of HAT-P-41b, detailed in Section 4.1. In Section 4.2 we present the measured center-of-transit times for these and previous transit observations of HAT-P-41b to determine the period of the planet, and in Section 4.3 we present the results of the UVIS G280 broadband light curves for the two visits and for each spectroscopic order using both systematic treatments.

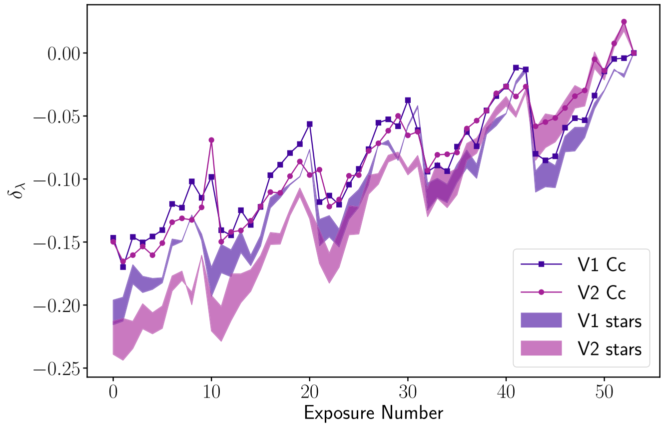

Figure 6. Changes in spectral position over the course of each visit, measured by cross-correlating to a template spectrum (points, Cc) and by fitting background sources on the full exposure image (shaded regions, stars). Each is shown relative to the final exposure for comparison. The spectral shifts are accounted for in the systematic treatment of each light curve.

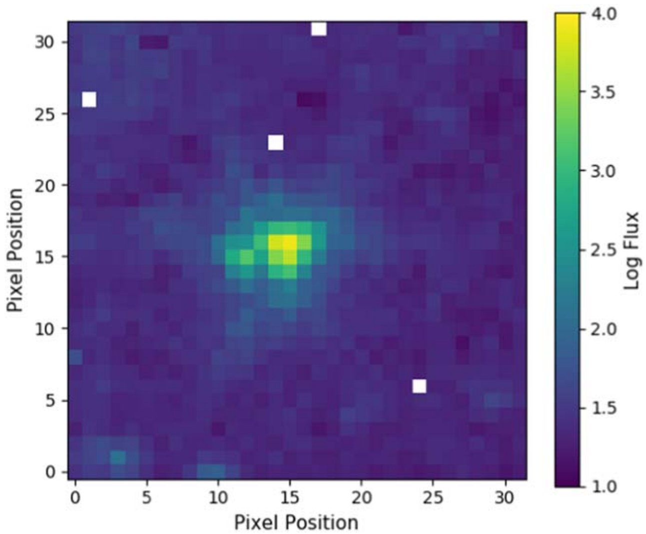

Figure 7. Mean flux in *Spitzer*'s 3.6 μm channel. Plotting on a logarithmic scale reveals HAT-P-41's faint, nearby companion at pixel position (12, 15). We limit our photometry aperture size to 2.25 pixels to minimize contamination from the companion. Bad pixels are masked in white.

4.1. Spitzer *Data Analysis*

Spitzer program 13044 (PI: D. Deming) acquired transit observations of HAT-P-41b at 3.6 and 4.5 μm on 2017 January 18 and 2017 February 3, respectively. The IRAC instrument (Fazio et al. 2004) acquired 32 $\times$ 32 pixel subarray frames at 2 second intervals in batches of 64. Each observation acquired a total of 21,632 frames over a span of $\sim$12 hr.

Using the POET pipeline (Stevenson et al. 2012; Cubillos et al. 2013), we apply a double-iteration, 4σ outlier rejection routine, 2D Gaussian centroiding, and 5$\times$ interpolated aperture photometry over a range of aperture sizes. We convert times to BJD_{TDB} using the JPL Horizons interface.

We find that the best aperture size (as defined by the lowest standard deviation of the normalized residuals) is 3.0 pixels; however, at this size there is noticeable contamination from the nearby binary companion. This is evidenced by the correlation between aperture size and transit depth (significant at 3.3σ). HAT-P-41's stellar companion is located $\sim$3 pixels away, in the wings of the primary star's point response function. This is shown in Figure 7, where we depict the mean flux at 3.6 μm on a logarithmic scale. We find that the impact of the stellar companion on the measured transit depth is minimal ($<1\sigma$) for apertures $\leqslant$2.25 pixels, and thus we adopt this value for our final analyses. We note that the transit time, inclination, and semimajor axis parameters do not vary with our choice of aperture size.

To derive our best-fit values (see Tables 1 and 2), we fit both *Spitzer* channels simultaneously using the transit model described by Mandel & Agol (2002), a linear trend in time, and a BLISS map (Stevenson et al. 2012) to account for intrapixel sensitivity variations. We estimate uncertainties using the differential-evolution Markov Chain Monte Carlo technique (ter Braak & Vrugt 2008) and test for convergence using the Gelmin–Rubin statistic (Gelman & Rubin 1992) by ensuring that the potential scale reduction factor is within 1% of unity. Figure 8 shows *Spitzer*'s normalized light curves and residuals. The best-fit 3.6 and 4.5 μm transit depths are 0.992% $\pm$ 0.008% and 1.028% $\pm$ 0.013%, respectively.

Table 1
Star and Planet Parameters Used in the Light-curve Fitting Process for This Analysis

Parameter	Value	Reference
Star		
V (mag)	11.087	Hartman et al. (2012)
M_* ($M_\odot$)	1.418	Hartman et al. (2012)
R_* ($R_\odot$)	1.786	Morrell & Naylor (2019)
$T_{\rm eff}$ (K)	6340	Morrell & Naylor (2019)
[Fe/H] (dex)	0.21	Hartman et al. (2012)
log(g)	4.14	Hartman et al. (2012)
Planet		
M_p (M_J)	0.795	Bonomo et al. (2017)
R_p (R_J)	1.685	Hartman et al. (2012)
Period (days)	2.69404861 $\pm$ 0.00000092	This work
T_0 (days)	2456600.29325 $\pm$ 0.00050	This work
Inclination (deg)	89.17 $\pm$ 0.62	This work
a/R_*	5.55 $\pm$ 0.04	This work
Eccentricity	0.0	Bonomo et al. (2017)

4.2. Updated Orbital Ephemeris

We used previous and current data to calculate an up-to-date orbital period for HAT-P-41b, including the ephemeris from the discovery (Hartman et al. 2012), as well as *HST* and *Spitzer* transit data (see Table 2). The *HST* data include the WFC3/UVIS transits where the +1 and −1 orders were treated independently (see Section 4.3), as well as WFC3/IR and STIS transits from the *Hubble* PanCET program (GO-14767, PIs D.K. Sing & M. Lopez-Moralez, K. Sheppard 2020, in preparation, private communication). We converted all of the available transit times to BJD_{TDB} using the tools from Eastman et al. (2010). These times were fit with a linear function of the period P and transit epoch E,

$$T(E) = T_0 + EP. \quad (5)$$

The resulting ephemeris is given in Table 2, with the linear function giving a reasonable fit to the data (see Figure 9), with a χ^2 value of 14.47 for nine degrees of freedom (DOF).

Table 2
Center-of-transit Times Used in Figure 9 to Calculate the Period of the Planetary Orbit as Well as the Resulting Best-fit Orbital Ephemeris

Instrument	Mode	Epoch (BJD_{TDB}) (days)	Note
		2454983.86247 ± 0.00107	Hartman et al. (2012)
HST WFC3-IR	G141	2457677.912139 ± 0.0008	
Spitzer IRAC	CH1	2457772.20477 ± 0.00021	
Spitzer IRAC	CH2	2457788.36879 ± 0.00027	
HST STIS	G430L	2458001.197547 ± 0.001151	visit 1
HST STIS	G430L	2458246.357040 ± 0.000339	visit 2
HST STIS	G750L	2458281.379682 ± 0.000363	
HST WFC3-UVIS	G280	2458332.566558 ± 0.000656	Visit 1, +1 order
HST WFC3-UVIS	G280	2458332.564321 ± 0.001366	Visit 1, −1 order
HST WFC3-UVIS	G280	2458335.260623 ± 0.000303	Visit 2, +1 order
HST WFC3-UVIS	G280	2458335.259912 ± 0.000290	Visit 2, −1 order
Period P (days)		T_0 (BJD_{TDB}) (days)	
2.69404861 ± 0.000000918		2456600.293253 ± 0.000504	

Note. All times have been converted to BJD_{TBD}.

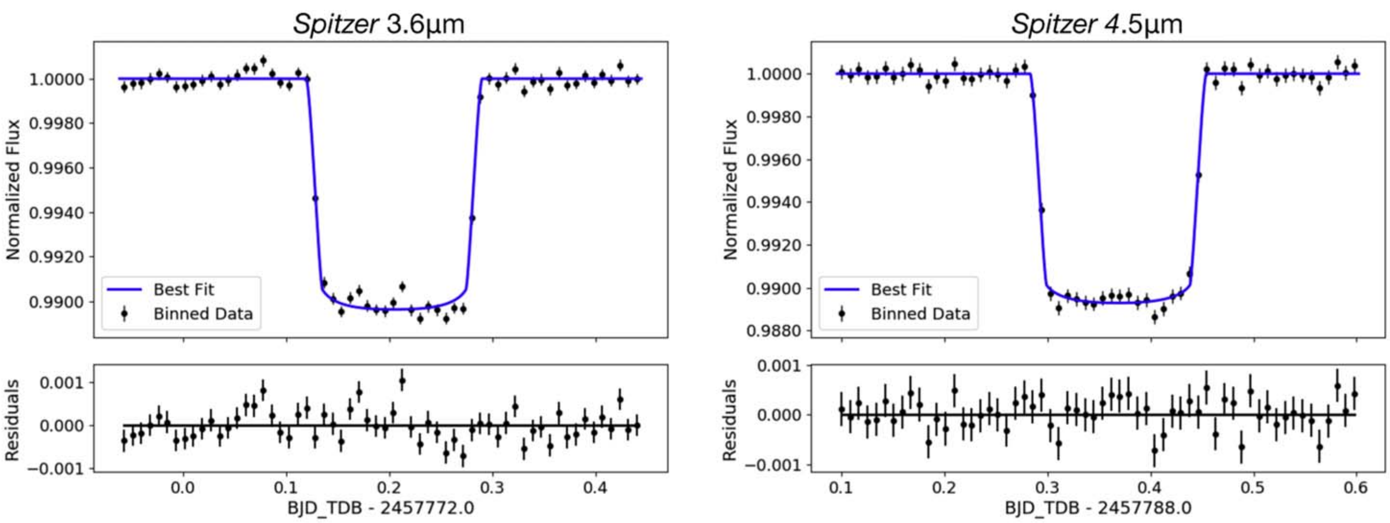

Figure 8. Transit light curves of HAT-P-41b using *Spitzer*'s 3.6 μm (left) and 4.5 μm (right) channels. We bin the data for plotting purposes only. The 3.6 μm residuals demonstrate a small amount of correlated noise at timescales shorter than the transit duration.

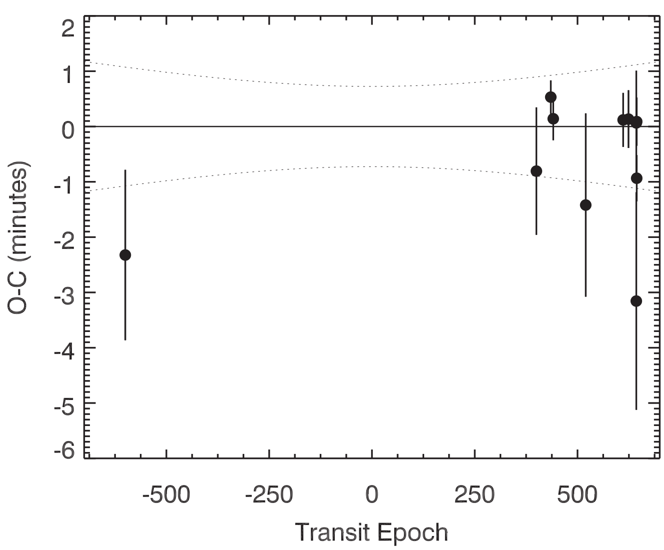

Figure 9. Observed minus calculated ($O-C$) diagram of measured HAT-P-41b transit times. The dashed line shows the 1σ uncertainty.

4.3. UVIS G280 Broadband Light-curve Results

We measure the broadband transit depth for UVIS G280 by summing the flux from 200 to 800 nm and correcting for systematics via systematic marginalization and jitter decorrelation independently for both visits and both spectral orders. We measure a combined transit depth of all four transit time-series measurements of $(R_p/R_*)^2 = 1.0406\% \pm 0.0029\%$ and $1.0330\% \pm 0.0033\%$, with an average standard deviation on the residuals of 221 ppm and 281 ppm, using the systematic marginalization and jitter decorrelation methods respectively. There is a 1.7σ difference between the two methods, likely due to the small differences between the uncertainties on each exposure for each analysis method that can be seen by comparing the bottom two panels of Figure 10. In each analysis we use the same extracted stellar spectra, the same limb-darkening coefficients derived using the 3D stellar models presented in Magic et al. (2015), and the same system parameters shown in Table 1.

We show the four transit light curves (two visits + two orders) corrected in Figure 10. The light curves shown have

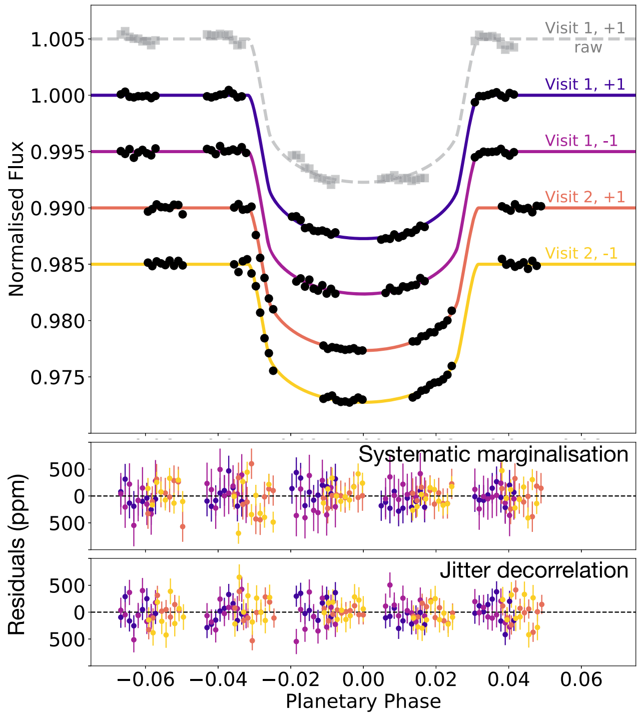

Figure 10. Top: broadband light curves. We show the raw extracted light curve for the visit 1, +1 spectral order to demonstrate the stability of the first *HST* orbit in the time series (light gray). The systematic corrected and normalized white-light curves for each visit and spectroscopic order (colored labeled points) are shown with the best-fit transit model. Each point represents a single exposure. Each light curve is offset for clarity. Middle: residuals from each light curve fit using the systematic marginalization method. Bottom: residuals for each light curve fit using the jitter decorrelation method. We measure the combined transit depth of HAT-P-41b to be $(R_p/R_*)^2 = 1.0406\% \pm 0.0029\%$ (standard deviation of the normalized residuals, SDNR = 221 ppm) and $1.0330\% \pm 0.0033\%$ (SDNR = 281 ppm), for each method respectively.

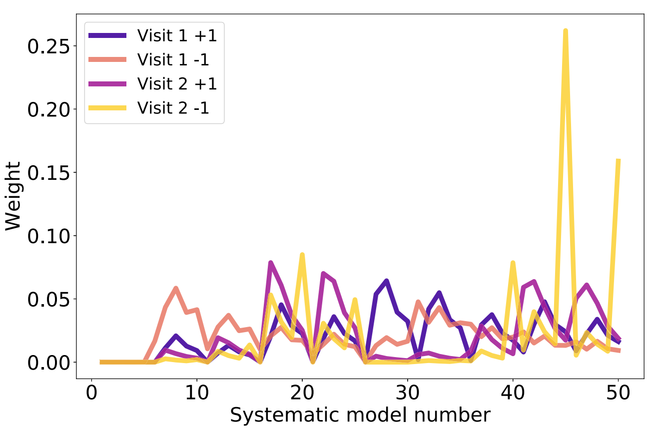

Figure 11. The evidence-based weight for each systematic model used in instrument systematic marginalization for each visit and order for the broadband light-curve analysis. The table of systematic models relating to each number can be found in Wakeford et al. (2016).

been corrected using the most favored model applied in systematic marginalization, with the underlying models derived from the same most-likely systematic model. For both data analysis methods—systematic marginalization and jitter decorrelation—the transit model is fit iteratively with the systematic model to measure the transit depth. We note that the light curves in Figure 10 only represent a portion of the information obtained through marginalization because all the information from corrected data using other weighted systematic models also goes into the final marginalized transit depth measurement (contribution weights can be seen in Figure 11). Using jitter decorrelation, we derive a single solution for the light-curve corrections and transit depth for each visit and spectral order. The individual light curves from jitter decorrelation are indistinguishable by eye from those from systematic marginalization presented here. For a more direct comparison we show the residuals of both systematic analyses at the bottom of Figure 10 with their related uncertainties; both achieve near photon noise precision.

While jitter decorrelation uses a fixed systematic model plus the jitter files directly from the telescope as a main decorrelation factor, systematic marginalization derives its information from evidence obtained from an array of independent systematic models. Systematic marginalization therefore accounts for the unknown factors affecting the light curves by weighting them according to the reduced data rather than the telescope's fine guidance sensors. Using systematic marginalization we find that each transit and spectral order favors a slightly different combination of systematic corrections. For visit 1 both orders predominantly favor models with a quadratic correction to δ_λ, while both orders of visit 2 favor a third-order ϕ_{HST} correction with additional correction for δ_λ. Given the similarity in the δ_λ trend for each visit and spectral order, as shown in Figure 6, the more favored correction of the *HST* breathing in visit 2 suggests that this movement on the detector is likely connected with the thermal effects of the telescope, and thus the corrections themselves are interchangeable in this specific case where the structure of the systematic is similar. For each light curve there is a marginal preference to correct for a linear trend in time across the whole visit; however, it is slightly more significant in visit 1. This linear trend across the whole visit has been noted in several other *HST* time-series observations (e.g., Deming et al. 2013; Kreidberg et al. 2014; Sing et al. 2015; Wakeford et al. 2016), and is thus likely related to the observatory as a whole rather than a specific instrument. For each visit and order we show the weighting assigned to each systematic model in the systematic marginalization reduction for the broadband analysis in Figure 11; these model weights are later applied to the spectroscopic light curves. The weights shown correspond to the systematic models shown in Table 2 of Wakeford et al. (2016). The structure of this grid is such that it first loops through polynomials correcting for δ_λ, followed by added corrections for ϕ_{HST}, with the second half of the grid (25–49) adding in corrections for ϕ_t. The overall structure of the computed weights shows that the corrections for δ_λ are the dominant factor given, causing the loop every four models.

5. Spectroscopic Analysis

To measure the transit depth as a function of wavelength and produce an atmospheric transmission spectrum for HAT-P-41b, we divide the stellar flux into 10 nm bins (∼5 detector resolution elements) from 200 to 800 nm. We note that it is possible to sample the transmission spectrum at a higher resolution (>2 resolution elements) in the most optimal portions of the spectrum where the flux is high; however, we use uniform bins across the whole wavelength range for consistency and accurate comparison.

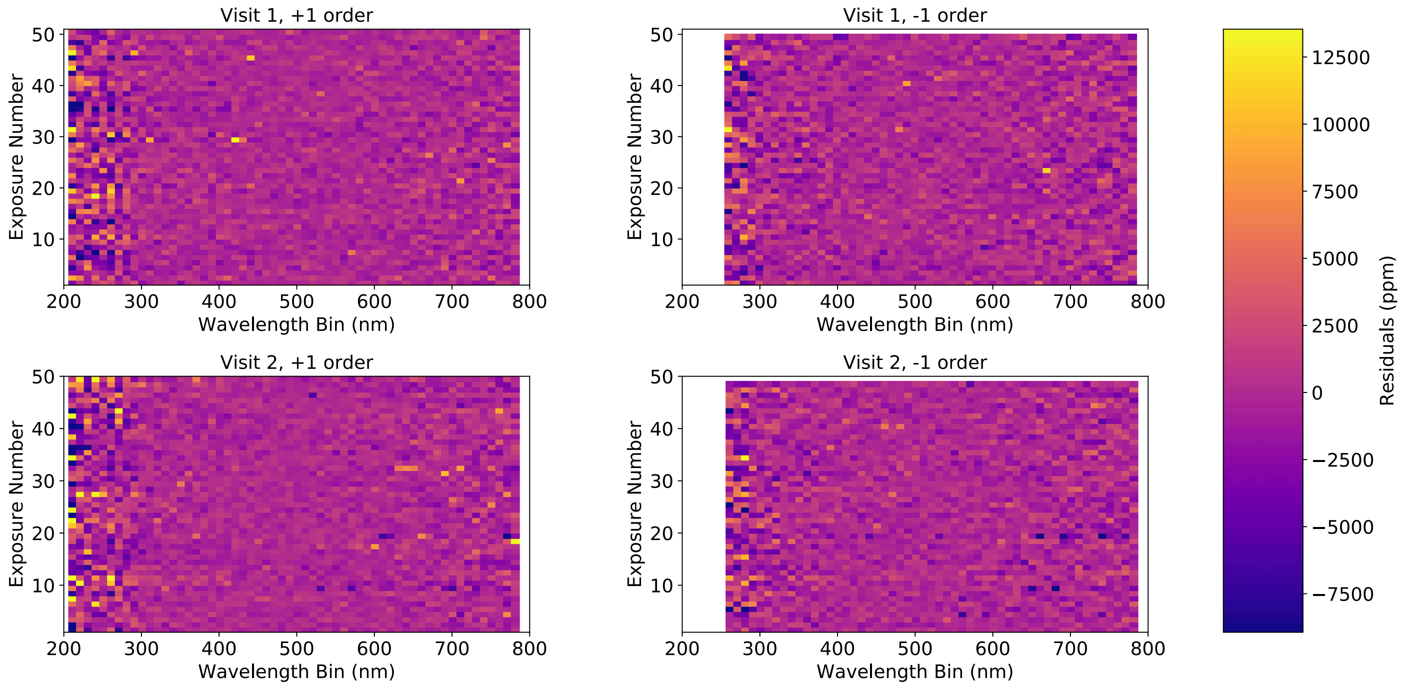

Figure 12. Intensity plot of the spectroscopic light-curve residuals for each wavelength bin using the systematic marginalization method. The color bar shows the residuals' amplitude for all intensity plots. For the −1 orders we do not compute the transmission below 250 nm because the flux is too low to produce convergent results in the systematic analysis.

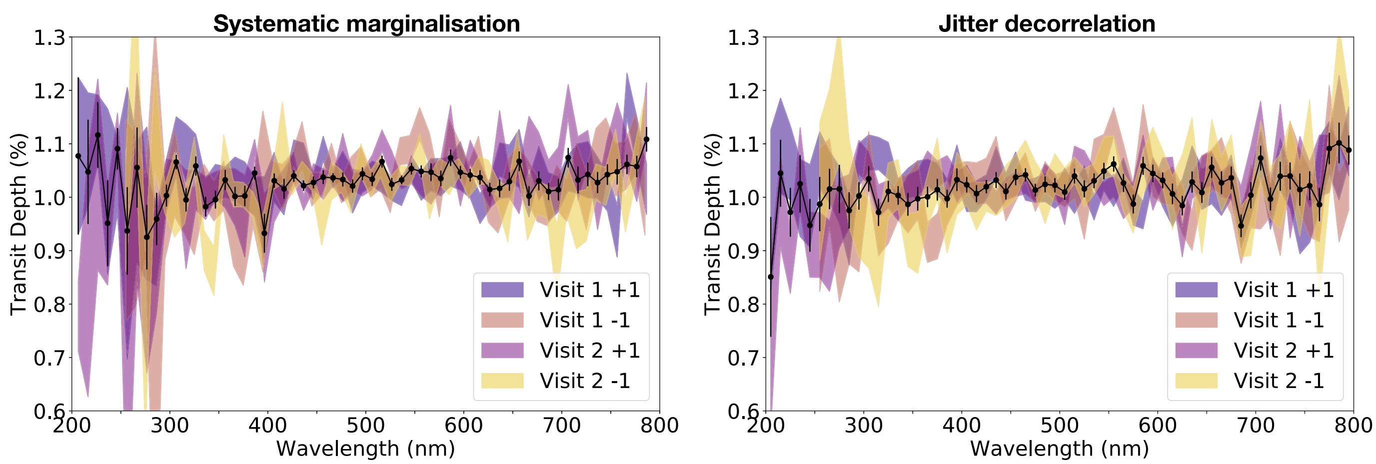

Figure 13. The individual and combined transmission spectra using both systematic marginalization and jitter decorrelation. The two visits and $+1/-1$ spectral orders are shown as colored shaded regions representing the range of the uncertainties for each spectrum. The final transmission spectrum combining the results of all four is shown as joined black points with error bars.

We analyze each individual spectroscopic light curve in the same way, as described in Section 4 for the broadband light curve, using both systematic marginalization and jitter decorrelation methods. In jitter decorrelation, the systematic correction model is unchanged between wavelength bins, thus assuming that all systematics are wavelength-independent. Using systematic marginalization, we account for any wavelength-dependent systematics by running the full grid of systematic models in each spectroscopic light curve. We then use the evidence-based weights for each of those models measured in the broadband light curve (see Figure 11) to marginalize over the measured values for each model in each light curve. By fixing the systematic model weightings to those derived from the broadband analysis, the uncertainty is then more representative of the dominant wavelength-independent systematics while incorporating the scatter measured across wavelength-dependent systematics being fit to the data.

Each visit and $+1/-1$ spectral order was analyzed separately using the parameters detailed in Table 1 to fix the period, inclination, and a/R_*, and using the center-of-transit times listed in Table 2. Using both jitter decorrelation and systematic marginalization independently, we find consistent results across both visits and spectral orders. Both methods reach photon noise precision in each of the channels as determined by calculating the white and red noise associated with the fits (see Pont et al. 2006), and finding a beta value of 1 consistent with no correlated noise. We show the

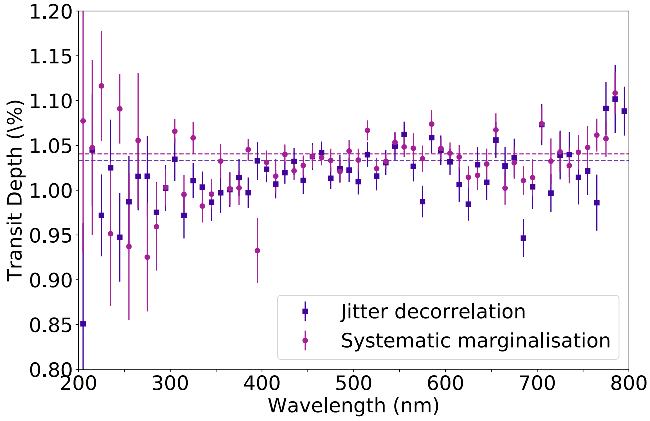

Figure 14. Direct comparison of the final combined transmission spectrum for each systematic treatment: jitter decorrelation (dark squares) and systematic marginalization (light circles). The horizontal dashed lines show the broadband depth measured using each method.

residuals from each of the spectroscopic light curves for the systematic marginalization analysis in Figure 12 as an intensity residual map to show any global structure in the fit. From the residuals it is clear that the −1 order light curves are noisier than the +1 orders. There is also an increase in the scatter at the edges of the wavelength regime, with shorter wavelengths dominating the overall noise range associated with the pure count rates measured from the stellar spectrum in each of the bins (see Figure 5).

In Figure 13, we present the transmission spectrum measured using both methods for each visit and each +/− first-order spectrum with the combined transmission spectrum overlaid. We show a direct comparison between the combined transmission spectra measured using the two systematic treatments in Figure 14, with 90% of the points overlapping at the 1σ uncertainty level. Table 3 lists the combined transit depth and uncertainty measured with each method along with the limb-darkening coefficients used in the fit. A direct comparison between the two methods is best demonstrated by looking at the standard deviation and uncertainty in the transit depth measured across the four transits analyzed (see Figure 15). It is again evident in the standard deviations and uncertainties that the lower counts measured in the near-UV wavelengths (<300 nm) introduce larger scatter and uncertainty to the transit depths. The standard deviation in the short wavelengths indicates that that derived transit depths in each light curve are more similar within the uncertainties using systematic marginalization rather than the jitter decorrelation method. However, there is added scatter with the marginalization method at longer wavelengths. The two methods have similar uncertainty profiles, indicating the ability to analyze these data with multiple methods. The unique contribution of the UV points to the transmission spectrum of an exoplanet atmosphere in combination with the optical data from a single observation with this low-resolution grism cannot be overstated.

6. Discussion

We present *HST*'s WFC3/UVIS G280 grism as a reliable observational mode to measure the transmission spectrum of exoplanet atmospheres from 200 to 800 nm, critically reaching down to near-UV and optical wavelengths not accessible to *JWST*. This wavelength range is important in order to understand and measure cloud opacity sources and their scattering profiles that are defined by the particle sizes (e.g., Lecavelier des Etangs et al. 2008; Wakeford & Sing 2015; Wakeford et al. 2017), escaping atmospheres (e.g., Ehrenreich et al. 2014; Sing et al. 2019), and absorption by Na.

To test this new mode, we measured the atmosphere of the hot Jupiter HAT-P-41b over the course of two consecutive transits with the WFC3/UVIS G280 grism. We obtained the positive and negative first-order spectra of the target star in each observation and extracted the stellar flux following the methods outlined by the UVIS calibration pipelines (Kuntschner et al. 2009; Rothberg et al. 2011; Pirzkal et al. 2017). We analyzed the transit data for each visit and spectral order using two well established techniques, instrument systematic marginalization (Wakeford et al. 2016) and jitter decorrelation (Sing et al. 2019). The two analysis techniques produced statistically similar transmission spectra for the atmosphere of HAT-P-41b. We obtain a precision of 29–33 ppm on the broadband transit depth from 200 to 800 nm, and an average precision of ≈200 ppm in 10 nm spectroscopic bins.

6.1. Comparison to STIS Observations

We compare the transmission spectrum of HAT-P-41b measured with WFC3/UVIS G280 grism to that measured using STIS G430L and G750L gratings. We find that the combination of the two *HST* observations in the G280 UVIS grism results in resolution and precision exceeding those of STIS, which required the combination of three *HST* observations to cover the whole wavelength range as opposed to two for UVIS. Figure 16 shows the transmission spectrum derived using systematic marginalization from two transits with UVIS G280 compared to the transmission spectrum from three transits with STIS G430L and G750L presented by K. Sheppard (2020, in preparation, private communication).

Assessing the overall use of UVIS G280 over the STIS gratings, there are a number of trade-offs to consider. G280 cannot be scanned and the throughput is much higher, so it will likely be more difficult to observe bright (Vmag < 7) targets, especially considering the impact of overlapping spectral orders that will make it difficult to extract individual spectral bins at this resolution. Therefore, bright targets will be more efficiently observed with STIS/G430L in particular. Additionally, although UVIS G280 can efficiently measure a wide wavelength range in a single observation it does not extend to wavelengths spanning the potassium absorption line, which can only be accurately captured with the STIS G750L grating. However, the extended wavelength coverage into the UV compared to the G430L grism and the comparable resolution mean that a potential Na line can be resolved just as easily with UVIS as with STIS, but with potentially higher precisions in UVIS. The measured UVIS spectrum far exceeds the resolution and precision over the comparative wavelengths that can be achieved by STIS/G750L (see Figure 16).

This direct comparison for the same planet demonstrates that the UVIS G280 grism can easily exceed the precision and resolution of STIS in an equivalent number of observations, while being more efficient and requiring less observing time. UVIS G280 also has the advantage of spanning the whole wavelength range in one shot, dramatically reducing the potential impact of stellar activity and systematics, which can cause offsets between data sets from different instrument modes. In summary, for targets with Vmag ⩾ 7 the UVIS G280 grism shows reduced systematics, higher resolution,

Table 3
Transmission Spectrum of HAT-P-41b Based on the Combined Spectrum of +1 and −1 Spectral Orders over Two Transit Events for Both Systematic Marginalization and Jitter Decorrelation

	Systematic Marginalization		Jitter Decorrelation		Limb-darkening Coefficients[a]			
Wavelength (nm)	Transit Depth (%)	Uncertainty (%)	Transit Depth (%)	Uncertainty (%)	c1	c2	c3	c4
200–800	1.04056	0.00293	1.03303	0.00331				
205	1.07731	0.14700	0.85089	0.11217	0.27642	−0.27861	0.17437	0.81199
215	1.04749	0.09769	1.04495	0.06266	0.44951	−1.31326	2.39714	−0.53880
225	1.11641	0.06163	0.97186	0.04573	0.26022	−0.34716	0.79494	0.26854
235	0.95137	0.08046	1.02503	0.05374	0.44189	−0.57725	1.16157	−0.07411
245	1.09086	0.03881	0.94739	0.04950	0.54045	−1.11394	2.37372	−0.82917
255	0.93706	0.08189	0.98717	0.05082	0.48574	−0.52757	1.52725	−0.54102
265	1.05554	0.07504	1.01539	0.03792	0.33614	−0.12161	1.23718	−0.49873
275	0.92522	0.06059	1.01556	0.04516	0.51787	−0.22060	0.71649	−0.07533
285	0.95923	0.04902	0.97523	0.03401	0.47085	−0.29824	1.30007	−0.53323
295	1.00307	0.02041	1.00242	0.02578	0.43969	−0.17729	1.45827	−0.79410
305	1.06577	0.01350	1.03449	0.02395	0.40399	0.12345	0.91689	−0.53110
315	0.99512	0.02188	0.97180	0.02567	0.34789	0.38909	0.43002	−0.26221
325	1.05841	0.01795	1.01076	0.01979	0.41584	0.42379	0.33271	−0.27752
335	0.98227	0.01837	1.00338	0.01746	0.32808	0.83687	−0.47180	0.19469
345	0.99562	0.01689	0.98657	0.02122	0.50090	0.47375	−0.04764	−0.04352
355	1.03245	0.01882	0.99715	0.02232	0.49485	0.49152	−0.08977	−0.02466
365	1.00155	0.01805	1.00064	0.01927	0.49130	0.55355	−0.23093	0.04401
375	1.00250	0.01921	1.01414	0.02044	0.51901	0.65211	−0.42396	0.11740
385	1.04525	0.01217	0.99727	0.01692	0.44683	0.40462	0.26623	−0.24303
395	0.93250	0.03636	1.03279	0.02120	0.48246	0.16780	0.44794	−0.21622
405	1.03092	0.01341	1.02334	0.01455	0.48142	0.45253	0.03247	−0.08316
415	1.01568	0.01890	1.00675	0.01593	0.43310	0.43124	0.12149	−0.10687
425	1.03996	0.01103	1.01964	0.01239	0.47865	0.31563	0.19400	−0.11728
435	1.02160	0.00993	1.03207	0.01504	0.50686	0.42439	−0.02042	−0.06239
445	1.02758	0.01111	1.01087	0.01519	0.62723	0.00768	0.49756	−0.26869
455	1.03755	0.01292	1.03748	0.01523	0.66796	−0.03296	0.39110	−0.16936
465	1.03632	0.00862	1.04188	0.01242	0.64089	0.10690	0.17586	−0.07282
475	1.03320	0.01313	1.01325	0.01207	0.68519	0.04928	0.14144	−0.03468
485	1.02089	0.01256	1.02408	0.01507	0.79901	−0.19234	0.36598	−0.16162
495	1.04370	0.01210	1.02236	0.01338	0.77433	−0.20489	0.40845	−0.15622
505	1.03363	0.01274	1.00958	0.01437	0.71140	−0.05044	0.22921	−0.08213
515	1.06672	0.01122	1.03961	0.01399	0.64107	−0.00460	0.31643	−0.15507
525	1.02409	0.01215	1.01568	0.01591	0.73764	−0.16794	0.39393	−0.17123
535	1.03226	0.00823	1.03075	0.01383	0.79821	−0.32921	0.54626	−0.23226
545	1.05347	0.01105	1.04898	0.01551	0.82715	−0.38564	0.54019	−0.20221
555	1.04829	0.01132	1.06219	0.01434	0.81141	−0.35516	0.49708	−0.18347
565	1.04683	0.01666	1.02657	0.01682	0.82890	−0.41148	0.54895	−0.20500
575	1.03509	0.01478	0.98730	0.01769	0.84535	−0.43068	0.52234	−0.18103
585	1.07381	0.01539	1.05872	0.01698	0.83910	−0.44512	0.56000	−0.20974
595	1.04651	0.01203	1.04453	0.01652	0.88137	−0.54670	0.63637	−0.22889
605	1.04134	0.01189	1.03169	0.01478	0.88844	−0.57180	0.65069	−0.23386
615	1.03707	0.01348	1.00632	0.01922	0.81257	−0.38094	0.42040	−0.13042
625	1.01444	0.01252	0.98434	0.01837	0.87418	−0.59117	0.70278	−0.27158
635	1.01662	0.01658	1.02845	0.01979	0.87714	−0.58646	0.66610	−0.24723
645	1.02919	0.01724	1.00875	0.01949	0.86284	−0.56322	0.65497	−0.25552
655	1.06727	0.01847	1.05593	0.02030	0.95153	−0.74127	0.72558	−0.26379
665	1.00227	0.01846	1.02700	0.02128	0.90248	−0.67572	0.74030	−0.27779
675	1.03065	0.01782	1.03617	0.02138	0.87733	−0.62328	0.65601	−0.22774
685	1.01072	0.01601	0.94646	0.02119	0.88769	−0.66447	0.70310	−0.25098
695	1.01402	0.02043	1.00378	0.02471	0.89369	−0.70395	0.75795	−0.27823
705	1.07414	0.01838	1.07324	0.02316	0.88686	−0.68657	0.72303	−0.26083
715	1.03237	0.02539	0.99668	0.02136	0.87414	−0.65906	0.67614	−0.23359
725	1.04279	0.02215	1.03922	0.02722	0.89617	−0.72378	0.74812	−0.26705
735	1.02738	0.01973	1.03978	0.02539	0.89467	−0.73795	0.77170	−0.28323
745	1.04238	0.01927	1.01427	0.03020	0.86509	−0.64972	0.65973	−0.23664
755	1.04771	0.02398	1.02146	0.02712	0.89132	−0.75184	0.79302	−0.29984
765	1.06149	0.01834	0.98611	0.03130	0.88774	−0.75638	0.78905	−0.29437
775	1.05751	0.02014	1.09123	0.02938	0.88279	−0.73219	0.73173	−0.25886
785	1.10846	0.02307	1.10165	0.03805	0.88973	−0.77932	0.81639	−0.31113

Note.
[a] Based on using the +1 order throughput curve and 3D stellar models from Magic et al. (2015).

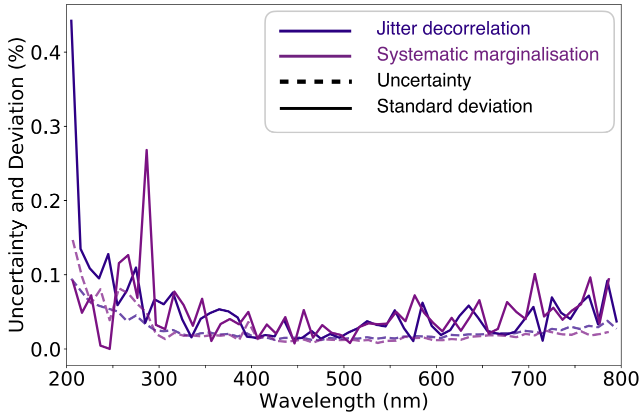

Figure 15. The standard deviation between the four individual transmission spectra in each wavelength bin for systematic marginalization (pink) and jitter decorrelation (purple).

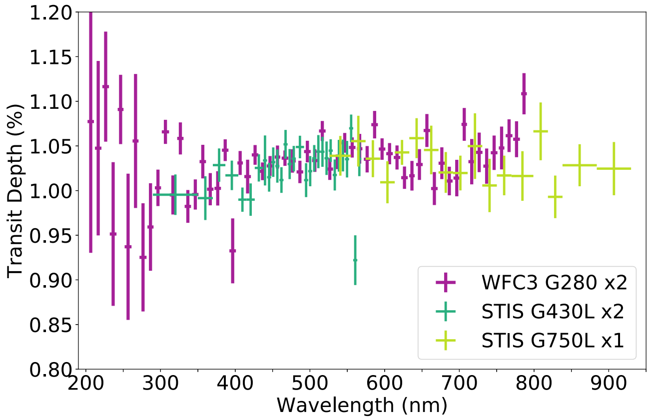

Figure 16. Transmission spectrum of HAT-P-41b measured with WFC3/UVIS G280 grism using systematic marginalization combining two *HST* observations (pink), compared to STIS G430L combined spectra from two *HST* observations (dark green) and one observation with the *HST* STIS G750L grating (K. Sheppard 2020, in preparation, private communication). The WFC3/UVIS G280 grism is able to efficiently measure the atmosphere of a transiting exoplanet from 200 to 800 nm to high precision, matching and exceeding that of STIS.

precision, and wavelength coverage with more efficient observing compared to STIS G430L and G750L gratings.

6.2. Searching for Evidence of Atmospheric Escape

The UVIS G280 grism has ideal wavelength coverage to search for signatures of atmospheric escape of Fe II at 240 and 260 nm, and the prominent Mg II doublet at 279.63 nm. A single resolution element for the G280 grism is ~2 nm, which encompasses the whole Mg II doublet absorption line, thus limiting us to strong, low-resolution detections. At a single resolution element of the detector, the scatter becomes large and we were unable to converge on a solution to fit the light-curve systematics. We therefore conducted an analysis of the HAT-P-41b transit data in 4 nm bins (two resolution elements) across 230–290 nm, with individual moving analyses in 10 nm steps to search for excess absorption from escaping ions. In this analysis, we find little significant evidence for additional absorption by Fe II and Mg II in the atmosphere. In a single 4 nm bin centered at 280 nm we measure 0.2% additional absorption compared to the average transit depth, which could potentially correspond to Mg II. However, this absorption is not seen in bins centered 10 nm either side of 280 nm that encompass the peak of the absorption. The scatter is of the order of 0.3% across the whole sampled range.

We conducted our search predominantly using the positive spectral orders for each visit because the throughput and flux levels are high enough for the precision needed at these wavelengths. However, for strong signatures such as those seen in WASP-121b (Sing et al. 2019) or KELT-9b (Hoeijmakers et al. 2018), which also orbit bright stars, the absorption signature will likely also be measurable in the negative order spectra as well. We conclude that there is no evidence of significant Fe II and Mg II escaping from the atmosphere of HAT-P-41b based on the precision of these measurements. However, we cannot currently conclude where this places HAT-P-41b in the comparative phase space because more measurements with this mode or similar to that shown in Sing et al. (2019) will be required over a wide temperature phase space to examine the likelihood of detection.

6.3. Planetary Specific Model Comparison

We ran each of the transmission spectra including the measured *Spitzer* transit depths through the planetary specific forward model grid for HAT-P-41b using rainout condensation presented by Goyal et al. (2018, 2019). In each case, the model fits have the same number of DOF, with the only additional fitting parameter being the absolute altitude of the model. For each UVIS G280 spectrum, we trim the first and last two data points, which are likely most affected by low flux and fringing, respectively, and append the *Spitzer* transit depths. Each transmission spectrum independently favors the same atmospheric model that has $T_{\rm eq} = 2091$ K, atmospheric metallicity [M/H] = +2.0, C/O = 0.7, 1100× scattering profile, and uniform cloud opacity = 0.2 (see Figure 17). We find $\chi^2_\nu = 1.45$ and 1.72 when fitting the most favored model to the jitter-decorrelated and marginalized transmission spectra, respectively.

The model shows prominent TiO/VO features in the near-UV fitting the UVIS G280 data well in the optical with a wavelength-dependent slope associated with a scattering opacity source composed of small sub-micron particles. This model predicts a muted H_2O feature in the near-IR that would be detectable with WFC3's G102 and G141 grisms. The *Spitzer* IR is dominated by CO_2, which would add additional constraints on the atmospheric metallicity (Moses et al. 2011) and can be validated by *JWST* NIRSpec observations.

7. Conclusions

We present *HST*'s WFC3/UVIS G280 grism as a new and ideal instrument mode for exoplanet time-series characterization. This is the first time that scientific analysis of any observation with this instrument mode has been published. As such, we provide a detailed breakdown of the challenges and advantages of the instrument, detailed instructions on the spectral extraction with reference to data files and programs provided through UVIS calibration files, and a comparative study of two well established systematic reduction methods.

To test the UVIS G280 grism for time-series data, we observed the transit of the hot Jupiter HAT-P-41b over two consecutive transit events. This allowed us to measure the overall stability of the instrument, the precision, and resolution

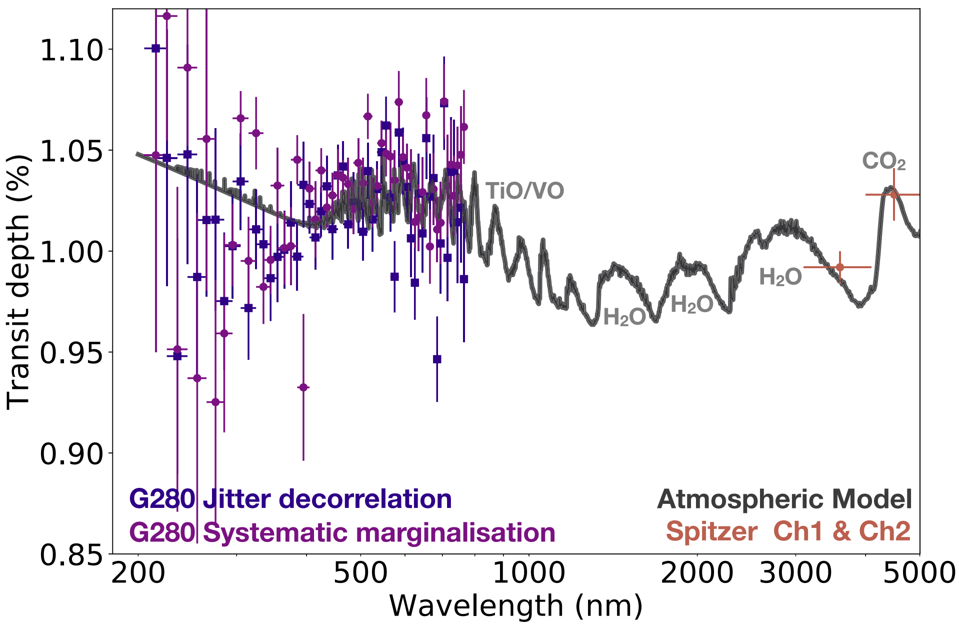

Figure 17. Transmission model fit using the planetary specific grid with rainout condensation by Goyal et al. (2018). Both the jitter-decorrelated and systematic marginalization G280 spectra were fit independently with the *Spitzer* data to the full grid of HAT-P-41b models. Both data sets found the same best-fit model with $T_{\rm eq}$ = 2091 K, [M/H] = +2.0, C/O = 0.7, 1100× scattering, cloud = 0.2.

without additional concerns associated with potential stellar activity. We obtained both positive and negative first-order spectra from each observation, providing four different data sets from 200 to 800 nm. We analyzed each data set separately before combining the information to produce the final atmospheric transmission spectrum of HAT-P-41b. We applied two different extraction and systematic analysis techniques to the data and find them to be statistically similar across the whole transmission spectrum, demonstrating the robust and consistent nature of the instrument critical for accurate studies of exoplanet transmission spectra.

We measure the complete transmission spectrum of the hot Jupiter HAT-P-41b from 200 to 800 nm in 10 nm bins and at 3.6 and 4.5 μm with *Spitzer*'s IRAC instrument. In the broadband UVIS light curves, we reach a precision of 29–33 ppm, with an average of ≈200 ppm in 10 nm wide spectroscopic channels. The transmission spectrum shows evidence of TiO/VO in the near-UV to optical with significant absorption from CO_2 in the *Spitzer* 4.5 μm channel. We fit a grid of forward models specifically derived for HAT-P-41b to the transmission spectrum from multiple reduction pipelines and find constant results with $T_{\rm eq}$ = 2091 K, [M/H] = +2.0, C/O = 0.7, scattering ×1100, and cloud opacity = 0.2 for rainout condensation (see Goyal et al. 2018, 2019). Additional measurements in the near-IR will further aid the interpretation of this planet's atmospheric transmission and will be detailed in future publications.

We demonstrate that *Hubble*'s WFC3 UVIS G280 grism is superior to the combination of STIS G430L and G750L gratings for time-series observations in terms of efficiency, precision, and resolution from 300 to 800 nm for exoplanet time-series observations. Notably, the UVIS G280 grism also allows access to wavelengths as short as 200 nm with the potential to measure the escaping atmosphere of giant exoplanets via Fe II and Mg II absorption lines and a broad range of other atmospheric processes. The wavelength coverage offered by the UVIS G280 grism (200–800 nm) provides a perfect complement to the spectroscopic capabilities of the *James Webb Space Telescope* (600–14,000 nm), and together they can probe the full extent of atmospheric processes in exoplanets that closely orbit their host star.

We thank D. Deming for use of data from his *Spitzer* program 13044[15] that provided the two transits used to obtain accurate system parameters. Thanks to S. Morrell for discussions on the stellar parameters with updates from *Gaia*. We acknowledge private communication from N. Nikolov and K. Sheppard for the STIS data analysis from the *Hubble* PanCET program (K. Sheppard 2020, in preparation, private communication).

This work is based on observations made with the NASA/ESA *Hubble Space Telescope*, HST-GO-15288,[16] that were obtained at the Space Telescope Science Institute, which is operated by the Association of Universities for Research in Astronomy, Inc. A portion of this work is based on observations made with the *Spitzer Space Telescope*, which is operated by the Jet Propulsion Laboratory, California Institute of Technology under a contract with NASA. H.R. Wakeford acknowledges support from the Giacconi Prize Fellowship at the Space Telescope Science Institute, which is operated by the Association of Universities for Research in Astronomy, Inc.

Software: POET pipeline (Stevenson et al. 2012; Cubillos et al. 2013), IRAF (Tody 1986, 1993), IDL Astronomy user's library (Landsman 1995), NumPy (Oliphant 2006), SciPy (Virtanen et al. 2019), MatPlotLib (Caswell et al. 2019), AstroPy (Astropy Collaboration et al. 2018), Photutils (Bradley et al. 2019).

[15] https://sha.ipac.caltech.edu/applications/Spitzer/SHA/#id=SearchByProgram&RequestClass=ServerRequest&DoSearch=true&SearchByProgram.field.program=13044&MoreOptions.field.prodtype=aor,pbcd&shortDesc=Program&isBookmarkAble=true&isDrillDownRoot=true&isSearchResult=true

[16] https://archive.stsci.edu/hst/search.php

Author Contributions

H.R. Wakeford led the UVIS data analysis with detailed comparisons provided by D.K. Sing. N. Pirzkal provided the UVIS calibration pipeline and knowledge of the instrument. K.B. Stevenson analyzed the *Spitzer* data and helped with discussions on the UVIS analysis. N.K. Lewis aided with the interpretation of the results and providing context for the observations. T.J. Wilson aided in the statistical analysis. All authors provided text and comments for the manuscript.

ORCID iDs

H. R. Wakeford https://orcid.org/0000-0003-4328-3867
D. K. Sing https://orcid.org/0000-0001-6050-7645
K. B. Stevenson https://orcid.org/0000-0002-7352-7941
N. K. Lewis https://orcid.org/0000-0002-8507-1304
T. J. Wilson https://orcid.org/0000-0001-6352-9735
J. Goyal https://orcid.org/0000-0002-8515-7204
T. Kataria https://orcid.org/0000-0003-3759-9080
T. Mikal-Evans https://orcid.org/0000-0001-5442-1300
N. Nikolov https://orcid.org/0000-0002-6500-3574

References

Astropy Collaboration, Price-Whelan, A. M., Sipőcz, B. M., et al. 2018, AJ, 156, 123
Bonomo, A. S., Desidera, S., Benatti, S., et al. 2017, A&A, 602, A107
Bourrier, V., Lecavelier des Etangs, A., Ehrenreich, D., et al. 2018, A&A, 620, A147
Bradley, L., Sipőcz, B., Robitaille, T., et al. 2019, astropy/photutils: v0.7.2, v0.7.2, Zenodo, doi:10.5281/zenodo.3568287
Caswell, T. A., Droettboom, M., Hunter, J., et al. 2019, matplotlib/matplotlib v3.1.0, v3.1.0, Zenodo, doi:10.5281/zenodo.2893252
Cubillos, P., Harrington, J., Madhusudhan, N., et al. 2013, ApJ, 768, 42
Cutri, R. M., Wright, E. L., Conrow, T., et al. 2012, Explanatory Supplement to the WISE All-Sky Data Release Products, http://wise2.ipac.caltech.edu/docs/release/allsky/expsup/index.html
de Wit, J., Wakeford, H. R., Gillon, M., et al. 2016, Natur, 537, 69
Deming, D., Wilkins, A., McCullough, P., et al. 2013, ApJ, 774, 95
Eastman, J., Siverd, R., & Gaudi, B. S. 2010, PASP, 122, 935
Ehrenreich, D., Bonfils, X., Lovis, C., et al. 2014, A&A, 570, A89
Evans, T. M., Sing, D. K., Goyal, J. M., et al. 2018, AJ, 156, 283
Fazio, G. G., Hora, J. L., Allen, L. E., et al. 2004, ApJS, 154, 10
Gelman, A., & Rubin, D. 1992, StaSc, 7, 457
Gilliland, R. L., Rajan, A., & Deustua, S. 2010, WFC3 UVIS Full Well Depths, and Linearity Near and Beyond Saturation, Instrument Science Report, WFC3 2010-10
Goyal, J. M., Mayne, N., Sing, D. K., et al. 2018, MNRAS, 474, 5158
Goyal, J. M., Mayne, N., Sing, D. K., et al. 2019, MNRAS, 486, 783
Hartman, J. D., Bakos, G. Á., Béky, B., et al. 2012, AJ, 144, 139
Helling, C. 2019, AREPS, 47, 583
Hoeijmakers, H. J., Ehrenreich, D., Heng, K., et al. 2018, Natur, 560, 453
Kreidberg, L., Bean, J. L., Désert, J.-M., et al. 2014, Natur, 505, 69
Kreidberg, L., Line, M. R., Parmentier, V., et al. 2018, AJ, 156, 17
Kuntschner, H., Bushouse, H., Kümmel, M., & Walsh, J. R. 2009, The Ground Calibrations of the WFC3/UVIS G280 Grism, ST-ECF Instrument Science Report, WFC3 2009-01
Landsman, W. B. 1995, in ASP Conf. Ser. 77, The IDL Astronomy User's Library, ed. R. A. Shaw, H. E. Payne, & J. J. E. Hayes (San Francisco, CA: ASP), 437
Lecavelier des Etangs, A., Pont, F., Vidal-Madjar, A., & Sing, D. 2008, A&A, 481, L83
Lothringer, J. D., Benneke, B., Crossfield, I. J. M., et al. 2018, AJ, 155, 66
Magic, Z., Chiavassa, A., Collet, R., & Asplund, M. 2015, A&A, 573, A90
Mandel, K., & Agol, E. 2002, ApJL, 580, L171
Marley, M. S., Ackerman, A. S., Cuzzi, J. N., & Kitzmann, D. 2013, in Comparative Climatology of Terrestrial Planets, ed. S. J. Mackwell et al. (Tucson, AZ: Univ. Arizona Press), 367
McCullough, P., & MacKenty, J. 2012, Considerations for using Spatial Scans with WFC3, STScI Instrument Science Report, WFC3 2012-08
McCullough, P. R., Crouzet, N., Deming, D., & Madhusudhan, N. 2014, ApJ, 791, 55
Morrell, S., & Naylor, T. 2019, MNRAS, 489, 2615
Moses, J. I., Visscher, C., Fortney, J. J., et al. 2011, ApJ, 737, 15
Nikolov, N., Sing, D. K., Pont, F., et al. 2014, MNRAS, 437, 46
Oliphant, T. 2006, NumPy: A Guide to NumPy (Spanish Fork, UT: Trelgol Publishing), http://www.numpy.org/
Pirzkal, N., Hilbert, B., & Rothberg, B. 2017, Trace and Wavelength Calibrations of the UVIS G280 +1/−1 Grism Orders, Instrument Science Report, WFC3 2017-20
Pont, F., Zucker, S., & Queloz, D. 2006, MNRAS, 373, 231
Rothberg, B., Pirzkal, N., & Baggett, S. 2011, First Results from Contamination Monitoring with the WFC3 UVIS G280 Grism, WFC3 Instrument Science Report, WFC3 2011-18
Sing, D. K., Fortney, J. J., Nikolov, N., et al. 2016, Natur, 529, 59
Sing, D. K., Lavvas, P., Ballester, G. E., et al. 2019, AJ, 158, 91
Sing, D. K., Pont, F., Aigrain, S., et al. 2011, MNRAS, 416, 1443
Sing, D. K., Wakeford, H. R., Showman, A. P., et al. 2015, MNRAS, 446, 2428
Stevenson, K. B., Harrington, J., Fortney, J. J., et al. 2012, ApJ, 754, 136
ter Braak, C., & Vrugt, J. 2008, Statistics and Computing, 18, 435
Tody, D. 1986, Proc. SPIE, 627, 733
Tody, D. 1993, in ASP Conf. Ser. 52, IRAF in the Nineties, ed. R. J. Hanisch, R. J. V. Brissenden, & J. Barnes (San Francisco, CA: ASP), 173
van Dokkum, P. G. 2001, PASP, 113, 1420
Virtanen, P., Gommers, R., Burovski, E., et al. 2019, scipy/scipy: SciPy 1.2.1, v1.2.1, Zenodo, doi:10.5281/zenodo.2560881
Wakeford, H., Sing, D., Deming, D., et al. 2013, MNRAS, 435, 3481
Wakeford, H. R., & Sing, D. K. 2015, A&A, 573, A122
Wakeford, H. R., Sing, D. K., Evans, T., Deming, D., & Mandell, A. 2016, ApJ, 819, 10
Wakeford, H. R., Visscher, C., Lewis, N. K., et al. 2017, MNRAS, 464, 4247
Wakeford, H. R., Wilson, T. J., Stevenson, K. B., & Lewis, N. K. 2019, RNAAS, 3, 7